Comparison of flexible array with laparoscopic transducer for photoacoustic-guided surgery

Jiaxin Zhang, Alycen Wiacek, Ziwei Feng, Kai Ding, Muyinatu Lediju Bell

Jiaxin Zhang, Alycen Wiacek, Ziwei Feng, Kai Ding, Muyinatu A. Lediju Bell, "Comparison of flexible array with laparoscopic transducer for photoacoustic-guided surgery," Proc. SPIE 12379, Photons Plus Ultrasound: Imaging and Sensing 2023, 1237910 (9 March 2023); doi: 10.1117/12.2656173

Event: SPIE BiOS, 2023, San Francisco, California, United States

Comparison of Flexible Array with Laparoscopic Transducer for Photoacoustic-Guided Surgery

Jiaxin Zhang[a], Alycen Wiacek[a], Ziwei Feng[a,b], Kai Ding[b], and Muyinatu A. Lediju Bell[a,c,d]

[a]Department of Electrical and Computer Engineering, Johns Hopkins University, USA
[b]Department of Radiation Oncology and Molecular Radiation Sciences, Johns Hopkins Medicine, USA
[c]Department of Biomedical Engineering, Johns Hopkins University, USA
[d]Department of Computer Science, Johns Hopkins University, USA

ABSTRACT

Photoacoustic imaging has recently demonstrated strong viability to visualize tool tips and assist with guidance during surgeries and interventional procedures. The more conventional rigid ultrasound transducers that can be used to sense photoacoustic signals require applied pressure for complete tissue contact when placed on curved surfaces. However, emerging flexible arrays are better suited to conform to different anatomical geometries. This work presents photoacoustic images acquired with a conventional laparoscopic transducer and a more flexible transducer array when placed in contact with surfaces of different curvatures, providing quantitative comparisons of image quality and transducer characterization. An optical fiber was inserted and translated within hemispherical phantoms along each transducer's elevation dimension to estimate the corresponding elevation field-of-view (FOV). A wider elevation FOV was measured with the flexible array, which indicates decreased elevation localization certainty, but increased ability to find tool tips when compared to the laparascopic probe. The average target depth accuracy was 99.36% with the flexible array and 95.05% with the laparoscopic probe, due to the differences in pressure required to maintain acoustic contact. Image contrast and signal-to-noise ratios were greater with the flexible array than with the laparoscopic probe. These properties of the flexible array enhance its desirability for photoacoustic-guided surgical interventions.

1. INTRODUCTION

Visualization and localization of surgical tool tips are essential components of photoacoustic-guided surgeries — an emerging image guidance technique that may be implemented to avoid accidental injuries to internal critical structures, including blood vessels, nerves, ureters, and cortical bone.[1,2] To visualize surgical tools, an optical fiber can be inserted inside or appended to the outside of interventional or surgical tools (e.g., needle tips,[3] catheter tips,[4] drill tips[5,6]). Ultrasound transducers may then be placed on the skull, spine, or abdominal structures to acquire photoacoustic raw data for guidance of neurosurgery,[7] spinal fusion surgery,[8,9] or liver surgery,[10] respectively.

Conventional ultrasound transducers are rigid with fixed array geometries, making them ideal for minimally varying surfaces. In particular, surgical laparoscopic ultrasound transducers have been employed to delineate biliary anatomy[11,12] or detect hepatic lesions during liver resection.[13] In laparoscopic photoacoustic imaging, new designs have been proposed for various surgical circumstances, such as attachment of diffusing fibers to the laparoscopic ultrasound probe,[14] affixation of a fiber bundle to a laparoscopic grasper tool,[15] or transducer assembly within a laparoscopic housing for photoacoustic nonlinear distortion correction.[16] In each case, the flexible laparoscopic probe contains a rigid acoustic sensor that can be deflected, thus applied pressure is necessary to maintain acoustic coupling contact.[11] This pressure causes organ distortions, tool tip localization difficulties, possible patient discomfort during interventions that lack anesthesia, and risks of injury to tissue.[17]

A flexible array is able to deform and provide complete contact on anatomical surfaces of varying curvatures.[18] This complete contact minimizes organ deformations, anatomical distortions, and patient discomfort and is expected to improve target localization and visualization. In addition, shape-sensing fiber attachments,[19] algorithms that estimate shape based on image sharpness[20] and entropy,[21] and deep neural networks for image

Photons Plus Ultrasound: Imaging and Sensing 2023, edited by Alexander A. Oraevsky, Lihong V. Wang, Proc. of SPIE Vol. 12379, 1237910 · © 2023 SPIE
1605-7422 · doi: 10.1117/12.2656173

formation[22] have been proposed to address associated challenges with inaccurate array geometry estimation and image reconstruction. Drawing on this promise, we recently presented the first known photoacoustic images and associated image assessments of a flexible array for photoacoustic-guided surgery.[23]

This paper compares the performance of the same flexible array transducer to that of a more conventional surgical laparoscopic probe. In particular, we experimentally estimate and compare field-of-views (FOVs) in the elevation dimension of each transducer to determine the ease of finding surgical tool tips. Comparisons of target size, target visibility, and target depth accuracy are also explored.

2. METHODS

2.1 Data Acquisition

A flexible array transducer (Japan Probe and Hitachi, Japan) and a laparoscopic transducer (Vermon, Tours, France) were each independently connected to the Vantage 128 ultrasound scanner (Verasonics Inc., WA, USA), with transducer parameters listed in Table 1. The ultrasound scanner was synchronized with a Phocus Mobile laser (Opotek, Inc., Carlsbad, CA, USA) emitting an optical wavelength of 750 nm through a 1 mm-core-diameter optical fiber, resulting in an average laser energy of 550 μJ per pulse at the tip of the fiber. This combination of optical and acoustic components comprised our photoacoustic imaging system for data acquisition.

To obtain photoacoustic images with the flexible array or the laparoscopic probe, two hemispherical plastisol phantoms were constructed with radii of curvature of 81.3 mm and 63.6 mm. Throughout this manuscript, these

Table 1. Flexible array and laparoscopic transducer parameters

Parameters	Flexible array	Laparoscopic probe
Number of Elements	128	128
Center Frequency	5 MHz	7.5 MHz
Element Width	0.8 mm	0.3 mm
Element Pitch	1.0 mm	0.6 mm
Element Height	10 mm	-
Elevation Aperture	10 mm	5 mm
Elevation Focus	100 mm	20 mm
Transmit Elements	64	32
Receive Elements	128	128

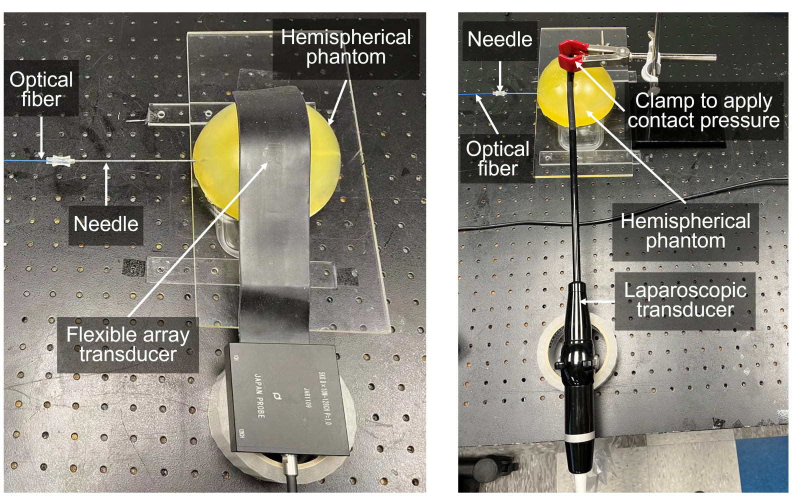

(a) (b)

Figure 1. Photographs of the experimental setups implemented to acquire images with (a) the flexible array and (b) the laparoscopic probe.

two phantoms will hereafter be referred to as the large and small phantoms, respectively. A hollow channel was bored in each phantom to insert a 2 mm-diameter needle housing the individual optical fiber at fixed depths of 40 mm in the large phantom and 50 mm in the small phantom. The flexible array and laparoscopic transducers were placed on the curved surfaces of phantoms to acquire raw photoacoustic channel data. The flexible array deformed, providing complete contact with the phantom surface without requiring applied pressure. When imaging with the laparoscopic probe, a stand with a clamp was used to apply additional pressure on the transducer to maintain complete contact with the curved phantom surface. Photographs of these experimental setups are shown in Fig. 1.

2.2 Image Reconstruction

Photoacoustic images were reconstructed using the conventional delay-and-sum (DAS) beamformer. The time delay τ for dynamic receive beamforming with the laparoscopic probe was computed as follows:

$$\tau_{i\_lap} = \frac{1}{c}\left[\sqrt{(x_f - x_i)^2 + (z_f - z_i)^2} - z_f\right] \tag{1}$$

where c is the speed of sound, (x_f, z_f) are the lateral and axial coordinates of the focal point, (x_i, z_i) are the lateral and axial coordinates of of the ith element. For the flexible array transducer, as the element positions vary according to different surface curvatures, time delays were calculated using the following equation:[23]

$$\tau_{i\_flex} = \frac{1}{c}\left\{\sqrt{\left[R\sin\left(\frac{P_i}{R}\right)\right]^2 + \left[z_f - R + R\cos\left(\frac{P_i}{R}\right)\right]^2} - z_f\right\} \tag{2}$$

where R is the radius of curvature of the hemispherical phantom (which is assumed to be the same curvature as the flexible array), and P_i is the distance between the ith element and the element that is perpendicular to the focal point. To form the final image, the DAS-beamformed signals were then envelope detected, followed by scan conversion and log compression.

2.3 Image Analysis

A 10 mm × 10 mm region of interest (ROI) was selected surrounding the photoacoustic target (i.e., the optical fiber tip) in each image. The z (i.e., axial) position associated with the maximum brightness within the ROI was defined as the target depth, D_t. To determine the target depth agreement with the ground truth, depth accuracy was defined as:

$$\text{Accuracy} = \left(1 - \frac{|D_t - D_g|}{D_g}\right) \times 100\% \tag{3}$$

where D_g is the ground truth depth of the center of the hollow channel in the phantom, based on the phantom construction design and post-construction caliper measurement verification.

Photoacoustic target size was measured as the full-width at half-maximum (FWHM) in lateral and axial image dimensions. Target visibility was assessed with contrast and signal-to-noise (SNR) measurements, calculated as:

$$\text{Contrast} = 20\log_{10}\left(\frac{\mu_t}{\mu_b}\right) \tag{4}$$

$$\text{SNR} = 20\log_{10}\left(\frac{\mu_t}{\sigma_b}\right) \tag{5}$$

where μ_t and μ_b are the means and σ_b is the standard deviation of the signal amplitudes (after envelope detection and scan conversion, prior to log compression) within ROIs placed at the same image depth within the photoacoustic target (denoted by subscript t) or within the background of the photoacoustic image (denoted by subscript b).

To approximate the elevation FOV, the elevation FWHM of the transducer was estimated by translating the optical fiber tip along the approximated elevation axis of the transducer. The optical fiber was fixed to a manual translation stage, which offers 15 mm of travel. The ultrasound probe was positioned to visualize the fiber tip in the photoacoustic image with the elevation dimension of the probe approximately parallel to the optical fiber. The fiber was translated in increments of 1 mm, and ten photoacoustic images were acquired at each fiber position. The maximum brightness in each of the ten photoacoustic images was calculated and plotted as a function of elevation fiber positions. The average of maximum brightness values for each of the fiber positions was plotted as a brightness curve, which was then normalized to the range [0, 1]. The FWHM was determined from this {normalized brightness curve, after linearly interpolating to increase the number of samples by a factor of 100 (i.e., resulting in a precision of 0.01 mm). When the optical fiber translation process produced an incomplete brightness curve with no clear minimum, the elevation FOV was determined based on the target visibility measurements (i.e., the minimum contrast and SNR within the elevation FOV) when imaging the same phantom with either probe.

3. RESULTS

Fig. 2 shows results obtained with the laparoscopic probe imaging the large phantom. In Fig. 2(a), photoacoustic images are presented in 10 mm $\times$ 10 mm ROIs with one example image shown for each stationary fiber position throughout the translation process. Qualitatively, the target is unclear at the 0 mm and 1 mm elevation positions (i.e., when the fiber tip was located off-axis relative to the imaging plane of the transducer). The target is qualitatively visible from positions 2 mm to 9 mm, when located within the elevation FOV of the laparoscopic transducer. At the 10 mm position, the target is no longer visible, as it is located outside of the elevation FOV. In Fig. 2(b), the distribution of the corresponding maximum brightness values in each of the 10 photoacoustic images for each of the 11 fiber positions is shown. The corresponding elevation FOV of the laparoscpic probe (i.e., the FWHM of the normalized brightness curve, as defined in Section 2.3) is 6.15 mm. Within this elevation FOV, the minimum contrast and SNR measured 8.81 dB and 47.42 dB, respectively, which were used to set the target visibility thresholds when defining the elevation FOV of the flexible array.

Fig. 3 shows results obtained with the flexible array imaging the large phantom. The photoacoustic target is qualitatively visible at all fiber positions during the translation process. In this case, a complete brightness curve was not possible with our setup. Thus, the 8.81 dB and 47.42 dB contrast and SNR thresholds described above were implemented to determine the elevation FOV of the flexible array. The contrast and SNR of the images obtained with the flexible array ranged 14.12-24.39 dB and 57.20-67.14 dB, respectively, which reside above the thresholds. Therefore, the elevation FOV of the flexible array is considered to be at least 14.00 mm at an image depth of 4 cm.

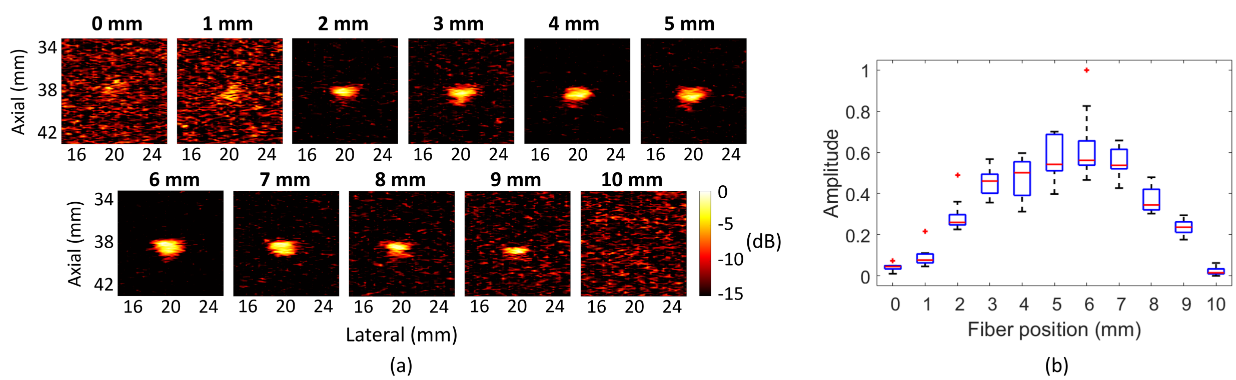

Figure 2. Results obtained with the large phantom and laparoscopic transducer. (a) Example photoacoustic images acquired at multiple stationary fiber positions during fiber translation in the elevation dimension of the transducer. (b) Box plots of brightness values associated with the translation process with the red horizontal denoting the median of the brightness values in the ten images at each stationary fiber position. The upper and lower box edges indicate the upper and lower quartiles, respectively. The maximum and minimum of the data set at each position are represented by the top and bottom horizontal lines of the whiskers. Outliers with maximum amplitude larger than 1.5 times the interquartile range are represented by the red crosses.

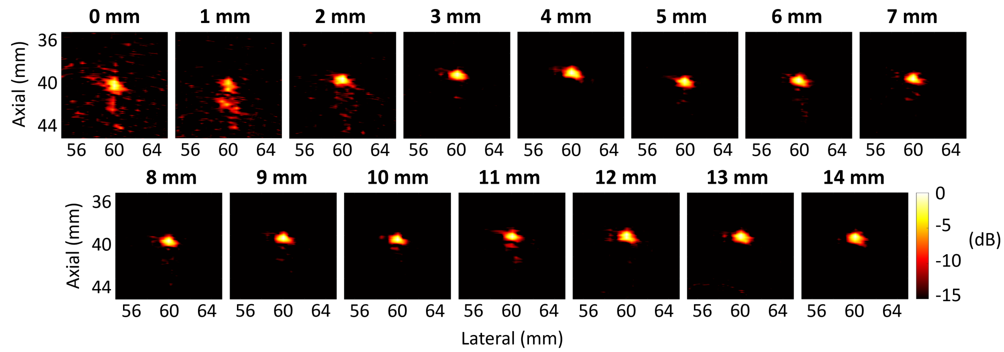

Figure 3. Example photoacoustic images acquired with the large phantom and flexible array transducer at multiple stationary fiber positions during fiber translation in the elevation dimension of the transducer.

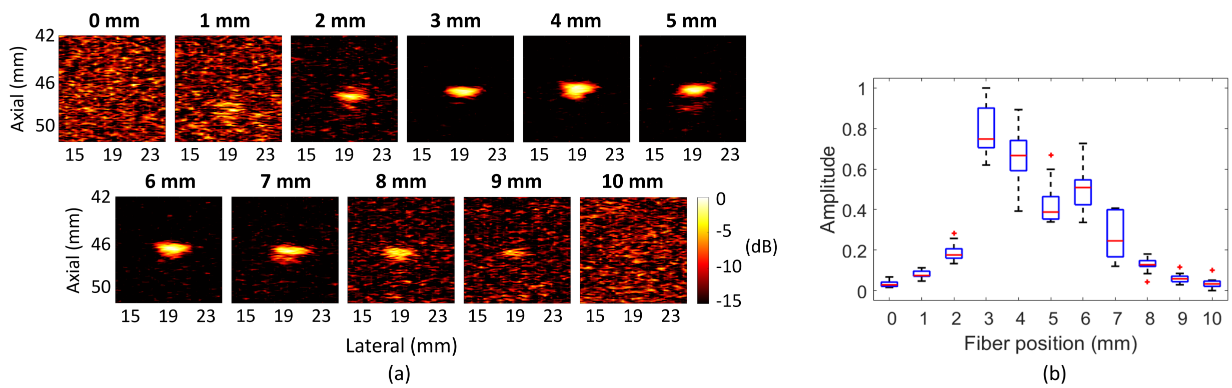

Figure 4. Results obtained with the small phantom and laparoscopic transducer. (a) Example photoacoustic images acquired at multiple stationary fiber positions during fiber translation in the elevation dimension of the transducer. (b) Box plots of brightness values associated with the translation process.

Fig. 4 shows results obtained with the laparoscopic probe imaging the small phantom. The photoacoustic target observed in Fig. 4(a) is qualitatively visible from positions 2 mm to 7 mm when located within the elevation FOV of the transducer. Fig. 4(b) shows the distribution of the corresponding maximum brightness values in each of the 10 photoacoustic images for each of the 11 fiber positions. The corresponding elevation FOV of the laparoscopic transducer is 4.05 mm.

Fig. 5 shows results obtained with the flexible array transducer imaging the small phantom. In Fig. 5(a), the target is qualitatively visible from positions 1 mm to 8 mm, when located within the elevation FOV of the transducer. In Fig. 5(b) shows the distribution of the corresponding maximum brightness values in each of the 10 photoacoustic images for each of the 11 fiber positions. The corresponding elevation FOV of the flexible array is estimated as 6.08 mm at an image depth of 5 cm.

Fig. 6 shows violin plots of photoacoustic image analysis results obtained within transducer elevation FOVs. The lateral and axial target size measurements with the flexible array and the laparoscopic probe are shown in Fig. 6(a). The greatest deviation from the 1 mm ground truth fiber-core-diameter is 3.19 mm, which occurs in the axial dimension when imaging the small phantom with the laparoscopic probe. Figs. 6(b) and 6(c) show comparisons of the image contrast and SNR, respectively for both the large and small phantom. In both the large and small phantoms, the median contrast with the flexible array exceeded the median contrast of the laparoscopic probe (i.e., 19.82 dB and 15.36 dB, respectively in the large phantom and 19.40 dB and 16.35 dB, respectively in the small phantom). Similarly, the median SNR with the flexible array exceeded the median SNR of the laparoscopic probe in both phantoms (i.e., 62.95 dB and 54.09 dB, respectively in the large phantom and 61.38 dB and 53.34 dB, respectively in the small phantom). Combined, these contrast and SNR measurements demonstrate improved target visibility with the flexible array when compared to the laparoscopic probe.

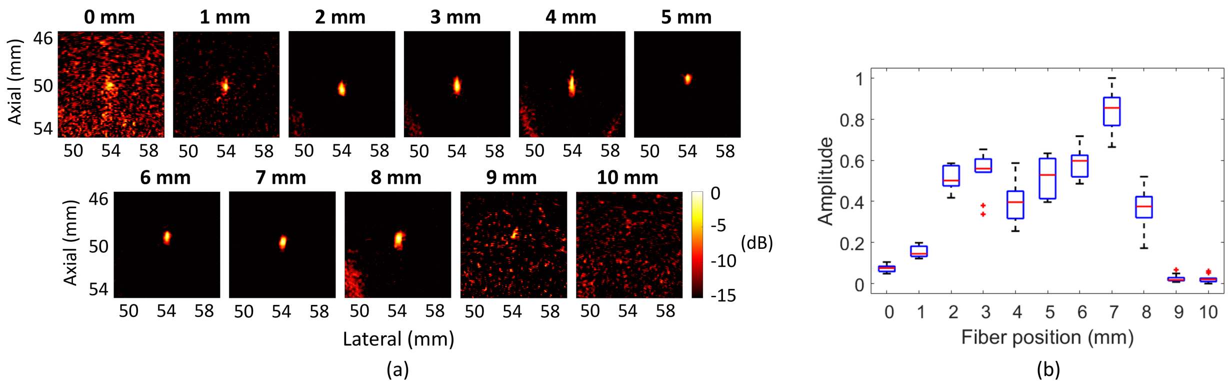

Figure 5. Results obtained with the small phantom and flexible array transducer. (a) Example photoacoustic images acquired at multiple stationary fiber positions during fiber translation in the elevation dimension of the transducer. (b) Box plots of brightness values associated with the translation process.

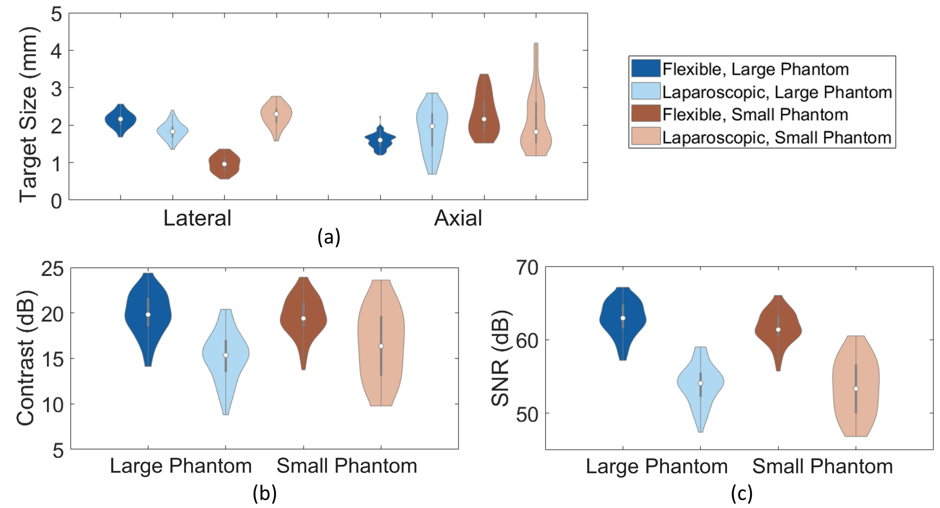

Figure 6. Violin plots of (a) measured target sizes, (b) contrast, and (c) SNR in large and small phantom experiments with the flexible array and the laparoscopic transducers. The shape of the shaded colors represent the probability density of the underlying data, each solid gray box denotes the interquartile range, and each open circle denotes the median.

In the large phantom (4 cm optical fiber depth), the average target depths measured from photoacoustic images acquired within the elevation FOVs were 40.34 mm and 38.29 mm with the flexible array and laparoscopic probe, respectively. These measurements correspond to 99.11% and 95.73% depth agreement with the ground truth, respectively. Similarly, in the small phantom (5 cm optical fiber depth), the average target depths within the elevation FOVs were 50.22 mm and 47.18 mm with the flexible array and laparoscopic transducer, respectively. These measurements correspond to 98.44% and 94.36% depth agreement with the ground truth, respectively. Overall, averaged over both the large and small phantoms, the average depth accuracy with the flexible array is 98.78% and that with the laparoscopic probe is 95.05%.

4. DISCUSSION

This paper presents the performance of a flexible array transducer relative to a more conventional surgical laparoscopic probe on two surfaces with different curvatures with three main findings. First, a wider elevational FOV was observed experimentally with the flexible array than with the laparoscopic probe. In particular, at 4 cm depth, the flexible array and laparoscopic probe have elevation FOVs of at least 14.00 mm and 6.15 mm, respectively. At 5 cm depth, these values were reduced to 6.08 mm and 4.05 mm, respectively. While elevation localization certainty is potentially lower (due to possible difficulties with determining if a tool tip is correctly aligned with the transducer imaging plane), these findings also indicate increased ability to localize surgical and interventional tool tips with the flexible array, which is highly desirable.

The second major observation is that better target depth agreement with the ground truth was achieved with the flexible array (i.e., 98.78%) when compared to that with the laparoscopic probe (i.e., 95.05%). This observation is attributed to the additional pressure required to image with the laparoscopic probe. This finding confirms our initial expectations that the accuracy of localizing surgical tool tips does not suffer from surrounding medium deformation when imaging with a transducer that contains a flexible array. This finding indicates that the flexible array is better suited to image registration with other imaging modalities that do not require deformation to obtain images (e.g., CT, MRI).

Third, better target visibility was achieved with the flexible array than with the laparoscopic probe (see Figs. 6(b) and 6(c)). This finding is promising when using a flexible array to assist with surgical guidance in challenging imaging environments (e.g., when visualizing structures in surrounding tissue despite poor optical or acoustic penetration, when seeking to avoid accidental injury to critical internal structures, or when differentiating multiple tool tips, blood vessels, or nerves).

In addition to the comparative benefits of the flexible array, we also observed deviations from the 1 mm ground truth target size (Fig. 6(a)) with both the flexible array and laparoscopic probe, which may be due to two possible factors. One possibility is that the optical fiber might not have been translated perfectly parallel to the elevation dimension of the transducer as intended, resulting in the lateral-axial imaging plane not being perfectly perpendicular to the translation trajectory, although this difference was imperceptible and therefore this factor is considered minimal. Otherwise, although results were presented as if the photoacoustic signal originated from the fiber tip, this signal might partially originate from the 2 mm-diameter metal needle surrounding the optical fiber.

Future work will focus on the registration of ultrasound and photoacoustic images, where ultrasound images present the surrounding tissue structures and photoacoustic images visualize and localize surgical tool tips to better guide surgeries. This is a promising direction because the flexible array and the laparoscopic probe employed in this work have transmit and receive elements which can be applied to both ultrasound and photoacoustic imaging modalities.

5. CONCLUSION

This paper is the first to compare the performance of a conventional laparoscopic transducer and a flexible array transducer when placed in contact with phantom surfaces of different curvatures to achieve photoacoustic images, resulting in quantitative comparative assessments. The flexible array utilized in this study has a wider elevation FOV than the traditional laparoscopic probe that was employed for the probe comparisons. The flexible array also achieved better target visibility and greater target depth agreement with the ground truth depth of the hollow channel prior to transducer placement for imaging, which bodes well for image registration with other modalities that do not require deformation (e.g., CT, MRI). These results are promising for the future introduction and deployment of flexible array transducers in photoacoustic-guided surgical interventions.

ACKNOWLEDGMENTS

This work was supported by NSF CAREER Award ECCS-1751522.

REFERENCES

[1] Lediju Bell, M. A., "Photoacoustic imaging for surgical guidance: Principles, applications, and outlook," *Journal of Applied Physics* **128**(6), 060904 (2020).

[2] Wiacek, A. and Bell, M. A. L., "Photoacoustic-guided surgery from head to toe," *Biomedical Optics Express* **12**(4), 2079–2117 (2021).

[3] Shubert, J. and Bell, M. A. L., "Photoacoustic based visual servoing of needle tips to improve biopsy on obese patients," in [*2017 IEEE International Ultrasonics Symposium (IUS)*], 1–4, IEEE (2017).

[4] Graham, M., Assis, F., Allman, D., Wiacek, A., Gonzalez, E., Gubbi, M., Dong, J., Hou, H., Beck, S., Chrispin, J., and Bell, M. A. L., "In vivo demonstration of photoacoustic image guidance and robotic visual servoing for cardiac catheter-based interventions," *IEEE Transactions on Medical Imaging* **39**(4), 1015–1029 (2019).

[5] Eddins, B. and Bell, M. A. L., "Design of a multifiber light delivery system for photoacoustic-guided surgery," *Journal of Biomedical Optics* **22**(4), 041011 (2017).

[6] Shubert, J. and Bell, M. A. L., "A novel drill design for photoacoustic guided surgeries," in [*Photons Plus Ultrasound: Imaging and Sensing 2018*], **10494**, 38–43, SPIE (2018).

[7] Graham, M. T., Huang, J., Creighton, F. X., and Bell, M. A. L., "Simulations and human cadaver head studies to identify optimal acoustic receiver locations for minimally invasive photoacoustic-guided neurosurgery," *Photoacoustics* **19**, 100183 (2020).

[8] Shubert, J. and Bell, M. A. L., "Photoacoustic imaging of a human vertebra: implications for guiding spinal fusion surgeries," *Physics in Medicine & Biology* **63**(14), 144001 (2018).

[9] Gonzalez, E. A., Jain, A., and Bell, M. A. L., "Combined ultrasound and photoacoustic image guidance of spinal pedicle cannulation demonstrated with intact ex vivo specimens," *IEEE Transactions on Biomedical Engineering* **68**(8), 2479–2489 (2020).

[10] Kempski, K. M., Wiacek, A., Graham, M., González, E., Goodson, B., Allman, D., Palmer, J. E., Hou, H., Beck, S., He, J., and Bell, M. A. L., "In vivo photoacoustic imaging of major blood vessels in the pancreas and liver during surgery," *Journal of Biomedical Optics* **24**(12), 121905 (2019).

[11] Bezzi, M., Merlino, P., Orsi, F., Di Nardo, R., Silecchia, G., Basso, N., Passariello, R., and Rossi, P., "Laparoscopic sonography during abdominal laparoscopic surgery: technique and imaging findings.," *AJR. American Journal of Roentgenology* **165**(5), 1193–1198 (1995).

[12] Buddingh, K. T., Nieuwenhuijs, V. B., van Buuren, L., Hulscher, J. B., de Jong, J. S., and van Dam, G. M., "Intraoperative assessment of biliary anatomy for prevention of bile duct injury: a review of current and future patient safety interventions," *Surgical Endoscopy* **25**(8), 2449–2461 (2011).

[13] Gagner, M., Rogula, T., and Selzer, D., "Laparoscopic liver resection: benefits and controversies," *Surgical Clinics* **84**(2), 451–462 (2004).

[14] Gao, S., Flegal, M. C., and Zhang, H. K., "Feasibility of laparoscopic photoacoustic imaging system based on diffusing side-illumination fibers," in [*Photons Plus Ultrasound: Imaging and Sensing 2022*], **11960**, 344–350, SPIE (2022).

[15] Wiacek, A., Wang, K. C., Wu, H., and Bell, M. A. L., "Photoacoustic-guided laparoscopic and open hysterectomy procedures demonstrated with human cadavers," *IEEE Transactions on Medical Imaging* **40**(12), 3279–3292 (2021).

[16] Lu, C., Xiong, K., Ma, Y., Zhang, W., Cheng, Z., and Yang, S., "Electrothermal-mems-induced nonlinear distortion correction in photoacoustic laparoscopy," *Optics Express* **28**(10), 15300–15313 (2020).

[17] Blaivas, M., Lyon, M., Brannam, L., Duggal, S., and Sierzenski, P., "Water bath evaluation technique for emergency ultrasound of painful superficial structures," *The American Journal of Emergency Medicine* **22**(7), 589–593 (2004).

[18] Nakahata, K., Tokumasu, S., Sakai, A., Iwata, Y., Ohira, K., and Ogura, Y., "Ultrasonic imaging using signal post-processing for a flexible array transducer," *NDT & E International* **82**, 13–25 (2016).

[19] Lane, C. J., "The inspection of curved components using flexible ultrasonic arrays and shape sensing fibres," *Case Studies in Nondestructive Testing and Evaluation* **1**, 13–18 (2014).

[20] Chang, J., Chen, Z., Huang, Y., Li, Y., Zeng, X., and Lu, C., "Flexible ultrasonic array for breast-cancer diagnosis based on a self-shape–estimation algorithm," *Ultrasonics* **108**, 106199 (2020).

[21] Noda, T., Tomii, N., Nakagawa, K., Azuma, T., and Sakuma, I., "Shape estimation algorithm for ultrasound imaging by flexible array transducer," *IEEE Transactions on Ultrasonics, Ferroelectrics, and Frequency Control* **67**(11), 2345–2353 (2020).

[22] Huang, X., Bell, M. A. L., and Ding, K., "Deep learning for ultrasound beamforming in flexible array transducer," *IEEE Transactions on Medical Imaging* **40**(11), 3178–3189 (2021).

[23] Zhang, J., Wiacek, A., González, E., Feng, Z., Ding, K., and Bell, M. A. L., "A flexible array transducer for photoacoustic-guided surgery," in [*2022 IEEE International Ultrasonics Symposium (IUS)*], 1–4, IEEE (2022).